Variable cell nudged elastic band method for studying solid–solid structural phase transitions

Guang-Rui Qian [a,d,e,∗], Xiao Dong [b], Xiang-Feng Zhou [b], Yongjun Tian [c], Artem R. Oganov [d,e,f], Hui-Tian Wang [a,b,∗∗]

[a] National Laboratory of Solid State Microstructures, Nanjing University, Nanjing 210093, China

[b] School of Physics and MOE Key Laboratory of Weak-Light Nonlinear Photonics, Nankai University, Tianjin 300071, China

[c] State Key Laboratory of Metastable Materials Science and Technology, Yanshan University, Qinhuangdao 066004, China

[d] Department of Geosciences, Stony Brook University, Stony Brook, NY 11794-2100, USA

[e] Department of Physics and Astronomy, Stony Brook University, Stony Brook, NY 11794-2100, USA

[f] Department of Geology, Moscow State University, Moscow 119992, Russia

ARTICLE INFO

ABSTRACT

The nudged elastic band (NEB) method, as a popular technique for studying reaction paths due to its efficiency, has not been extensively used in solid state physics because of the need to deal with the variation of the unit cell during solid–solid transformations. Here we present an extended technique—a variable-cell NEB (VC-NEB) technique combined with the *ab initio* method, implemented in the USPEX code. Our technique is applied to reconstructive solid–solid phase transitions of GaN: from wurtzite to rocksalt (B4 → B1) and from zincblende to rocksalt (B3 → B1). As a more challenging application, we study the mechanism of the recently predicted insulator–metal phase transition of BH. The results reveal that the VC-NEB technique is an efficient and general method and should have wide applications for studying the paths and mechanisms of reconstructive phase transitions. Results of the VC-NEB method can be considered as a starting point for a more sophisticated treatment using the transition path sampling method, the main prerequisite of which is to have an initial transformation trajectory.

© 2013 Elsevier B.V. All rights reserved.

1. Introduction

Phase transitions determine many aspects of the behavior of materials—famous examples are tin pest (which allegedly played a fatal role in Captain Scott's expedition to the South Pole, and also in Napoleon's invasion of Russia) and the shape memory effect (e.g. in nitinol NiTi). It is essential to reveal possible mechanisms behind structural phase transitions for understanding the behavior of materials [1].

A phase transition process can be considered as a double-ended problem, in which the algorithm is required to locate the intermediate states. As is well known, the nudged elastic band (NEB) [1–3], as a widely used method for solving double-ended problems, is an efficient and robust approach for seeking the reaction paths and the saddle points along the "minimum energy path" (MEP) on

the potential energy surface between the two endpoints. The NEB method has been successfully applied to molecular chemical reactions [2], surfaces [3], and defect migration [4], in particular it could provide the energy barrier between the given initial and final states of a phase transition process. Some improvements have been presented to enhance the robustness and to raise the efficiency of the NEB method [3–7]. However, most of the problems treated by the NEB method are considered under the constraint of a constant unit cell, which is reasonable for the above mentioned problems, but is not suitable for studying the phase transition mechanisms (which require the variation of the unit cell along the transition path). The solid-state NEB (SSNEB) approach [8] has been developed and applied to the solid-state phase transitions, but the lattice deformation and the displacement of atoms are treated independently within the rapid nuclear motion approximation. Recently, a generalized solid-state NEB (G-SSNEB) method proposed by Sheppard et al. [9] has investigated the solid–solid transformations involving the unit-cell and atomic degrees of freedom, using a scaled stress with a Jacobian term along the steepest-descent direction and the atomic forces.

We here develop a somewhat different formulation, which is referred to as the variable cell NEB (VC-NEB) method, treats the

cell and atomic coordinates on an equal footing and operates in an expanded configuration space under the constant pressure condition. Our VC-NEB method within the first principles framework has been added to the USPEX code as a new part [10]. The VC-NEB method is a more general tool for exploring the activation paths between the two endpoints of a phase transition process within a larger configuration space.

2. Variable cell nudged elastic band method

As in the traditional NEB method, a set of images $\{X_1, X_2, \ldots, X_u, \ldots, X_n\}$ connecting the two endpoints X_1 and X_n are used to describe the transition path in the VC-NEB method, where X_u is a vector containing the coordinates of the uth image in a special configuration space. Employing the forces orthogonal to the path and the "virtual" springs between the images, finally the image chain would converge to the true MEP to seek the transition routes. In contrast to the NEB method, the VC-NEB method expands the configuration space and the force vectors, which has components from the cell and atomic positions transformed to have the same dimensionality. In contrast to the G-SSNEB method, the VC-NEB method has as its salient feature that the expanded force vectors are always along the gradient of the expanded potential energy surface, which is of great importance for finding the true MEPs.

We describe the unit cell of a crystal by using the variable matrix, which is determined by the matrix of lattice vectors $\mathbf{h} = \{a, b, c\}$, with a cell volume of $\Omega = \det(\mathbf{h})$. In the variable cell technique [11–13], the finite strain tensor $\bar{\bar{\varepsilon}}$ as a free variable is always chosen, instead of the lattice vector $\mathbf{h}$, for the sake of convenience. Thus we can replace $\mathbf{h}_0$ as a reference configuration by $\mathbf{h} = (1 + \bar{\bar{\varepsilon}})\mathbf{h}_0$, where $\bar{\bar{\varepsilon}}$ includes nine components ε_{ij} ($i, j = 1, 2, 3$). The atom fractional coordinates r_v ($v = 1, 2, \ldots, N$) indicate the positions of the vth atom among the total N atoms in the unit cell. The full configuration space is described by the vector $\mathbf{X} = (\varepsilon_{1i}, \varepsilon_{2i}, \varepsilon_{3i}; r_1, \ldots, r_N)$ ($i = 1, 2, 3$), with $9 + 3N$ components.

Under the applied pressure P, the enthalpy $H = E + P\Omega$ is determined by the $(9+3N)$-dimensional potential energy surface—the "enthalpy surface"

$$H = H(\varepsilon_{1i}, \varepsilon_{2i}, \varepsilon_{3i}; r_1, \ldots, r_N), \tag{1}$$

where E is the energy of this structure. The expanded "force vector" in a $9 + 3N$ configuration space can be defined by the derivative of the enthalpy with respect to $\mathbf{X}$ as follows

$$\mathbf{F} = -\left.\frac{\partial H}{\partial \mathbf{X}}\right|_P. \tag{2}$$

The strain components of $\mathbf{F}$ on the lattice are the derivatives of H with respect to

$$f_{(\bar{\bar{\varepsilon}})} = -(\sigma + P\Omega)(1 + \bar{\bar{\varepsilon}}^T)^{-1}, \tag{3}$$

where σ is the quantum-mechanical stress tensor [14] at a given configuration $\mathbf{X}$. The forces on atoms, $f_1, f_2, \ldots, f_N$, can be obtained from the Hellmann–Feynman theorem [15]. Finally, the general force $\mathbf{F}$ can be written as [11]

$$\mathbf{F} = (f_{(\bar{\bar{\varepsilon}})}, gf_1, \ldots, gf_N)^T, \tag{4}$$

where the metric tensor $g = \mathbf{h}^T\mathbf{h}$ is introduced to keep the symmetry during structure relaxation [11,13].

The tangent vector τ along the path in the NEB method is represented as the unit vector to neighboring images [2,3]. The transverse components of the potential forces acting on the lattices and atoms are respectively defined as $f_{(\bar{\bar{\varepsilon}})}^{\nabla\perp}$ and $f_v^{\nabla\perp}$. The nudging spring forces on lattices and atoms to keep the image spacings are $f_{(\bar{\bar{\varepsilon}})}^{s\parallel}$ and $f_v^{s\parallel}$. We can now define the VC-NEB force $\mathbf{F}^{\text{VC-NEB}}$, the cell force
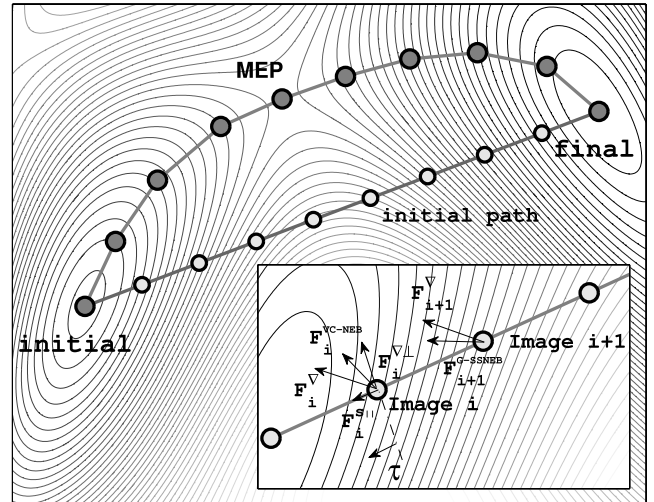

Fig. 1. The minimum energy path (line with gray cycle) and initial path are described on the enthalpy surface. The forces in the VC-NEB method on Image i are shown in the inset. $\mathbf{F}_i^{\nabla}$ is the potential force in the gradient direction. $\mathbf{F}_i^{\nabla\perp}$ and $\mathbf{F}_i^{s\parallel}$ are the transverse component of $\mathbf{F}_i^{\nabla}$ and the spring force, respectively. The forces on Image $i + 1$ indicate the differences between the potential force $\mathbf{F}^{\nabla}$ and $\mathbf{F}^{\text{G-SSNEB}}$ in the G-SSNEB method.

$f_{(\bar{\bar{\varepsilon}})}^{\text{VC-NEB}}$ acting to reshape the new image of the cell, and the atom force $f_v^{\text{VC-NEB}}$ shifting the atoms

$$f_{(\bar{\bar{\varepsilon}})}^{\text{VC-NEB}} = f_{(\bar{\bar{\varepsilon}})}^{s\parallel} + f_{(\bar{\bar{\varepsilon}})}^{\nabla\perp}, \tag{5}$$

$$f_v^{\text{VC-NEB}} = f_v^{s\parallel} + f_v^{\nabla\perp}, \tag{6}$$

$$\mathbf{F}^{\text{VC-NEB}} = \left(f_{(\bar{\bar{\varepsilon}})}^{\text{VC-NEB}}, gf_1^{\text{VC-NEB}}, \ldots, gf_N^{\text{VC-NEB}}\right)^T. \tag{7}$$

In the VC-NEB method, the basic idea is to search the MEPs by studying the "enthalpy surface" instead of the "potential energy surface" [16] in the traditional NEB method. When applying the VC-NEB method to reconstructive phase transitions, the activation path is determined by finding the MEPs on the enthalpy surface in a larger $(9 + 3N)$-dimensional configuration space, combining the unit cell and atomic variables.

The images along the path are relaxed to MEPs through $\mathbf{F}^{\text{VC-NEB}}$, which contain the transverse components of the potential forces $\mathbf{F}^{\nabla\perp}$ and the spring forces $\mathbf{F}^{s\parallel}$ (Fig. 1). The VC-NEB and G-SSNEB methods treat the problem in different metric spaces [17] and have a significant technical difference. In the VC-NEB method, all the components of the general forces are along the gradient direction on the enthalpy surface, whereas in the G-SSNEB method they are replaced by the true lattice force (the derivative of energy). For the latter, the computation is implemented under the assumption of an isotropic elastic medium with a Poisson ratio of zero, while this assumption is not needed in our VC-NEB method.

3. Implementation of the VC-NEB method

The code is distributed (available on request from G.R. Qian) as a new part of the USPEX package [10]. We will describe the procedure of the VC-NEB calculations below.

Before performing a VC-NEB calculation for a phase transition process with two given endpoint images, its initial path is defined by a set of intermediate images, which are generated by a linear interpolation between the initial and final states or the user-provided specific configurations.

By starting from the initial path, the images are relaxed to the MEP through the VC-NEB force $\mathbf{F}^{\text{VC-NEB}}$, which is derived from the
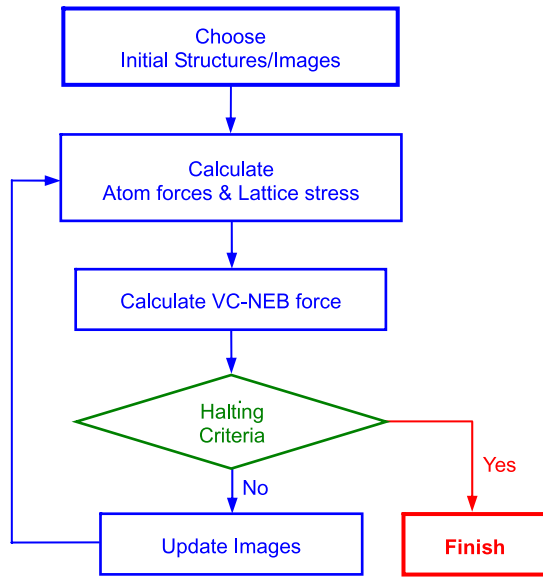
Fig. 2. (Color online) Basic procedure of the VC-NEB technique.

Table 1
Structure parameters of B4, B3 and B1 structures for GaN at zero pressure. Other calculated and experimental values are also given for comparison.

Phase	a (Å)	c/a	u	P_t (GPa)	B_0 (GPa)	B_0'
B4	3.123	1.629	0.377	45.7	170.6	4.34
	3.180[a]	1.632[a]	0.376[a,c]	42.9[a]	237[a]	4.2[a]
	3.145[c]	1.633[c]	0.377[a]	43.7[b]	245[a]	3.2[a]
	3.160–3.190[a]	1.622–1.632[a]		44.5[c]	188[a]	
				33.5[d]		
B3	4.542			45.0	173.2	4.36
	4.497[a]			42.1[a]	196[a]	4.2[a]
	4.49–4.52[a]			35.4–65[a]	190[a]	
B1	4.263	1.414	0.5		218.9	4.15
	4.225[a]				240[a]	4.5[a]
	4.180[c]				248[a]	5.5[a]
					323[a]	3.8[a]

[a] Ref. [40] and references therein.
[b] DFT-LDA (ABINIT code) in Ref. [41].
[c] DFT-LDA (VASP code) in Ref. [28].
[d] DFT-LDA (PWSCF code) in Ref. [24].

force and stress tensors calculated by the popular *ab initio* codes including Quantum ESPRESSO [18] and VASP [19]. The variable-elastic-constant, improved-tangent-estimate and climbing-image NEB schemes [2–4] are also implemented in our VC-NEB code for the accurate saddle point determination. The VC-NEB calculation will stop when the user-defined convergence conditions on force and enthalpy have been satisfied.

The basic procedure of the VC-NEB technique is as follows, as shown in Fig. 2:

(1) Firstly, we rearrange the lattice vectors and the sequence of atoms with a rotation-avoiding approach in the initial and final images, which will be further discussed in Section 6.

(2) Initialize the first set of images, based on the linear interpolation between the initial and final images or with the user-provided specific configurations, for the intermediate images.

(3) Calculate the stress on the lattice and the forces on the atoms in the intermediate images from first principles.

(4) Calculate the VC-NEB forces based on the stress on the lattice and the forces on the atoms by determining the tangent vector τ with the vector $\mathbf{X} = (\varepsilon_{1i}, \varepsilon_{2i}, \varepsilon_{3i}; r_1, \ldots, r_N)$ $(i = 1, 2, 3)$ for intermediate images.

(5) Calculate the transformation strain of the cell and displacement of atoms based on the VC-NEB forces by using the optimization algorithm, and generate a new set of images.

(6) Repeat steps (3)–(5) until the halting criteria are satisfied.

4. Illustration of VC-NEB and phase transitions in GaN

In recent years, many theoretical models have been presented to explore phase transitions from wurtzite to rocksalt (B4 → B1) [20–28] and from zincblende to rocksalt (B3 → B1) [22,29–35] in II–VI, III–V and IV binary semiconductors. For the pressure-induced B4 → B1 phase transition, two representative *hexagonal* and *tetragonal* transition paths have been proposed. For the pressure-induced B3 → B1 phase transition, based on the least-enthalpy calculation [31], the Landau-like model [32] and the extended uniaxial Bain path method [35], the *Imm*2 symmetry as an intermediate activated state has been found. We revisit the B4 → B1 and B3 → B1 phase transitions in GaN by using the VC-NEB technique.

All calculations were performed in the framework of density functional theory by using the Quantum ESPRESSO code [18] and

the PW91 exchange-correlation functional (GGA family) [36]. The electron–ion interactions are described by ultrasoft pseudopotentials, [37] with the $1s^2$ core configuration for the N atoms and the [Ar] core configuration for the Ga atoms. The kinetic energy cut-off for the plane wave expansion is 75 Ry and the k-point set is an $8 \times 8 \times 6$ grid of the reciprocal unit cell with a Γ-centered Monkhorst–Pack grid [38]. The common tangent construction [39] was used to predict the B4 → B1 and B3 → B1 transition pressures P_t in GaN. The results indicate $P_t = 45.7$ and 45.0 GPa, for B4 → B1 and B3 → B1, respectively, which are in good agreement with the previously theoretical and experimental values, as listed in Table 1.

For the VC-NEB method, in the first step, we should calculate the exact configurations of the two endpoint phases, by minimizing the enthalpy at constant pressure. In order to ensure the robustness of the VC-NEB method and to find the precise saddle point, the improved techniques presented in Refs. [2,3] (including variable-elastic-constants, improved-tangent-estimate and climbing image NEB) are also utilized in our VC-NEB code. For all the VC-NEB calculations in this work, we take 27 intermediate images. For the halting criteria for performing the VC-NEB method, we choose 0.03 eV/Å for the root-mean-square (RMS) force convergence (but 0.01 eV/Å at saddle point) for the images. The spring constant is within a range of 0.2–1.5 eV/Å^2, which is slightly narrower than that suggested in Ref. [2].

4.1. B4 → B1 phase transition

GaN as an important semiconductor shows remarkable properties for technological applications [42,43]. As is well known, GaN undergoes a B4 → B1 phase transition under pressure. This phase transition process is in general summarized by two paths (*hexagonal* [21–25] and *tetragonal* [20–26]). As shown in Fig. 3, both paths can be considered as two-stage processes with the coordination number changing from 4 to 6. A pair of particular free parameters (u, γ) is used to describe the structures. Based on the calculation methods as mentioned above, under the transition pressure $P_t = 45.7$ GPa, the parameters u for the B4 and B1 phases are 0.377 and 0.5, respectively, in good agreement with the values reported in the literature, as listed in Table 1.

For performing the VC-NEB calculation of the B4 → B1 phase transition, we should focus on the detailed information on the saddle point, including the image position and the enthalpy barrier. First, by using the linear interpolation for all the dimensions of $\mathbf{X}$ between the B4 and B1 phases, we generate the primary 27 intermediate images. After performing the VC-NEB procedure, we find the candidate transition path through the optimization. The
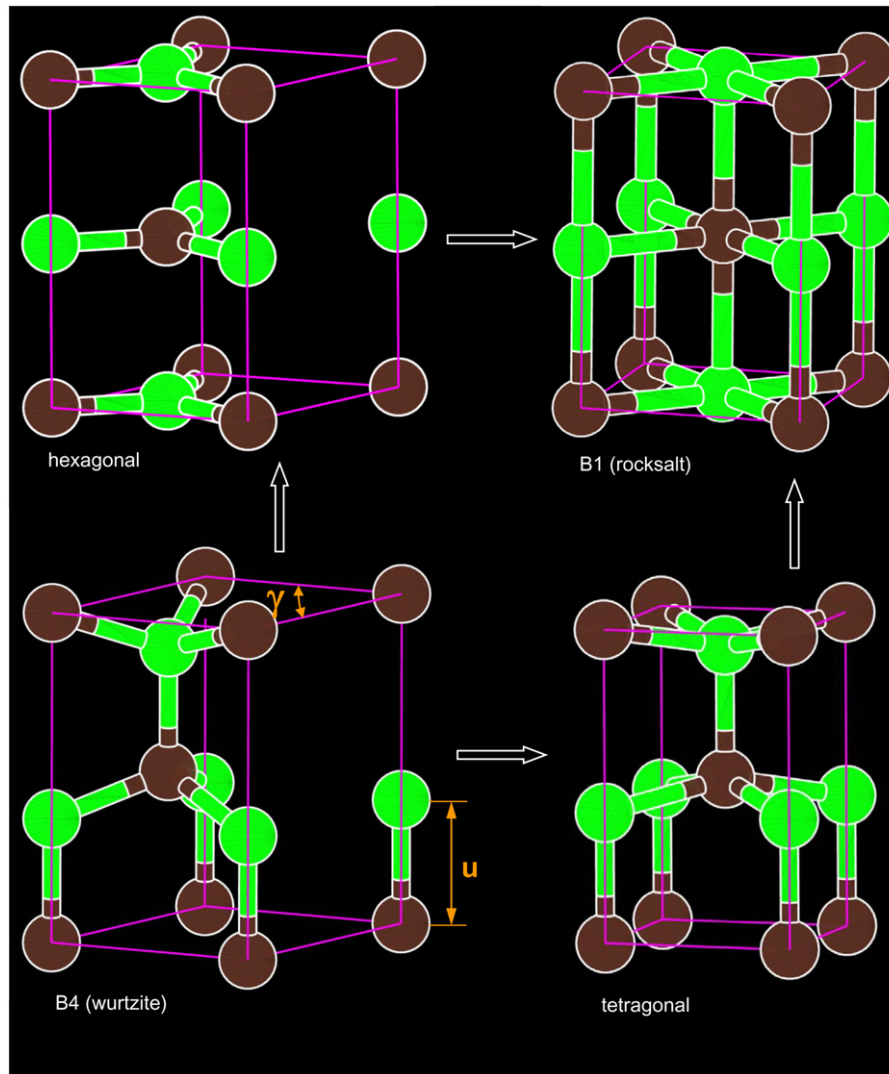
Fig. 3. (Color online) Two representative paths for B4 → B1 phase transition, through the *hexagonal* and *tetragonal* intermediate structures, respectively. The structural parameters (u, γ) denote the primary characteristics of these structures.

results of the *tetragonal* path, as plotted in Figs. 4 and 5, show the dependence of the enthalpy H and the internal structural parameters (u, γ) on the image number. Without the rotation-avoiding technique (discussed in Section 5), as shown in Fig. 4, the enthalpy H has no change within the first six images (or the last five images), implying that the structure belongs still to the B4 (or B1) type. Therefore the first five images and the last four images could be avoided during calculation with the rotation-avoiding technique to increase the number of "effective" images as shown in Fig. 5. On implementing the rotation-avoiding technique in the VC-NEB calculation, a transformation enthalpy barrier of 0.34 eV/formula is found at Image 15 in Fig. 5(a), which is close to 0.384 eV/formula in Ref. [28] and 0.37 eV/formula in Ref. [22]. As shown in Fig. 5(b), γ changes from 60° at the initial image to 90° at Image 23 and u increases from 0.377 to 0.427 during the lattice deformation. From Image 23 to Image 29, u increases from 0.427 to 0.5 and H decreases from 0.14 eV/formula to 0, while γ remains at 90°, implying that there indeed exists a *tetragonal* intermediate phase with a coordination number of 5. At the final state (Image 29), H, u and γ are 0°, 0.5° and 90°, respectively, indicating that the B4 (wurtzite) phase has transformed into the B1 (rocksalt) phase.

We now explore the *hexagonal* intermediate phase path and compare with the *tetragonal* path. The initial set of other intermediate images is generated by using the linear interpolation

between the B4 and B1 structures and assigned to be the *hexagonal* structure. Starting from the assigned initial path, the VC-NEB calculation reveals the existence of another possible transition path, as shown in Fig. 6. From the initial structure to Image 12, H increases from 0 to 0.31 eV/formula and u changes from 0.377 to 0.5, while γ keeps at 60°, correspondingly the crystal structure changes from the B4 structure into the *h*-MgO structure with the coordination number of 5. From Image 12 to Image 29, u remains at 0.5 while γ increases from 60° to 90°, and the crystal structure transforms to the B1 structure. Following this transition path, the B4 → B1 transition goes through a *hexagonal* intermediate phase and must overcome an enthalpy barrier of 0.39 eV/formula at Image 20. The transformation enthalpy barrier along the *hexagonal* path is 0.05 eV/formula higher than that along *tetragonal* path, indicating that the tetragonal path should be preferred for the B4 → B1 phase transition in GaN.

To confirm the universality of the VC-NEB method, we also perform similar calculations for the B4 → B1 phase transitions in ZnO and AlN. The results validate that ZnO also favors the tetragonal path. The phase transition happens at a pressure $P_t = 9.54$ GPa with a barrier of ∼0.13 eV/formula, which is very close to the value reported in Ref. [23]. For the B4 → B1 phase transition along the tetragonal path, the tetragonal ZnO is a metastable structure. For the B4 → B1 phase transition in AlN, the hexagonal path should be
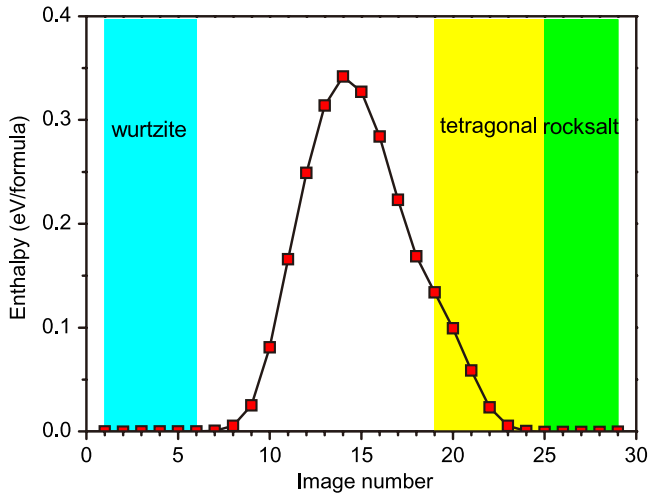
Fig. 4. (Color online) Enthalpy barrier for GaN B4 → B1 transformation at the equilibrium pressure $P_t = 45.7$ GPa along the "tetragonal" path. Without the rotation-avoiding technique, the structure transformation process starts from Image 6 and finishes at Image 25, implying that there are only 18 "effective" intermediate images on the phase transition path.
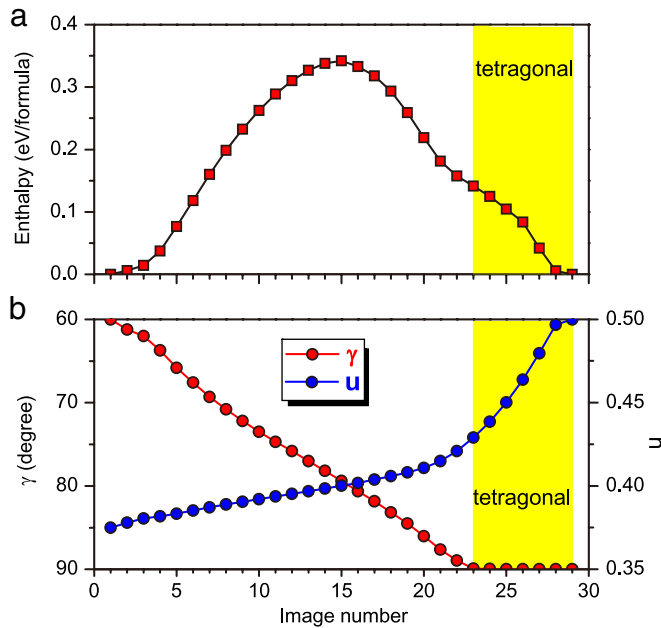

Fig. 5. (Color online) Enthalpy barrier and evolution of internal structural parameters for the B4 → B1 phase transition of GaN at the transition pressure along the "tetragonal" path. The saddle point is at Image 15 with a barrier of 0.34 eV/formula.

Fig. 6. (Color online) Enthalpy barrier and internal structural parameters for the B4 → B1 phase transition of GaN under transition pressure along the *hexagonal* path with a barrier of 0.39 eV/formula.

Fig. 7. (Color online) Enthalpy barriers for the B4 → B1 phase transition of AlN at transition pressure along *hexagonal* path, by using the VC-NEB and G-SSNEB methods [44].

the unique transition path, because when exploring the path starting with the tetragonal intermediate images, the optimized transition path converges into the hexagonal path quickly, never finding an MEP in the tetragonal intermediate images. For AlN, the *h*-MgO structure is a metastable intermediate structure, as shown in Fig. 7. Our results are in good agreement with the findings of Ref. [28]. In particular, the pathway obtained by the VC-NEB method is similar to the one given by using the G-SSNEB method, and with the same transition state structure.

4.2. B3 → B1 phase transition

The VC-NEB method can also give a clear picture for the B3 → B1 phase transition in GaN from the zincblende (B3) structure to the rocksalt (B1) structure. We assume for the moment that
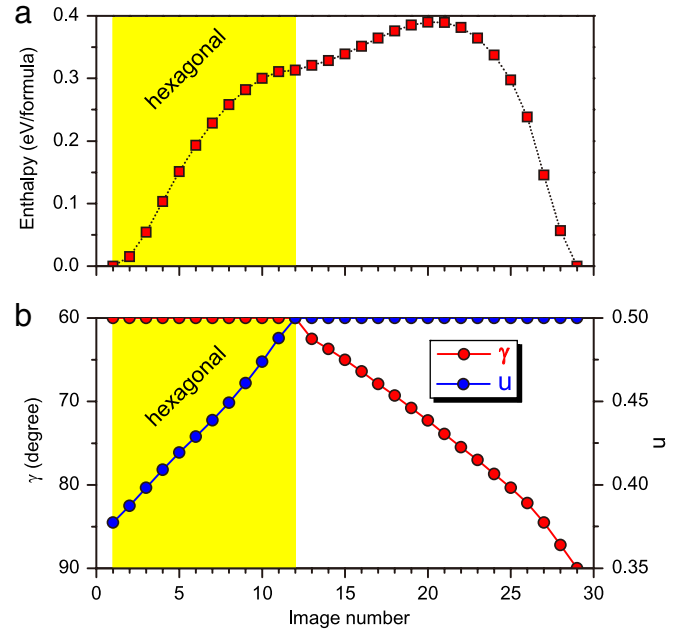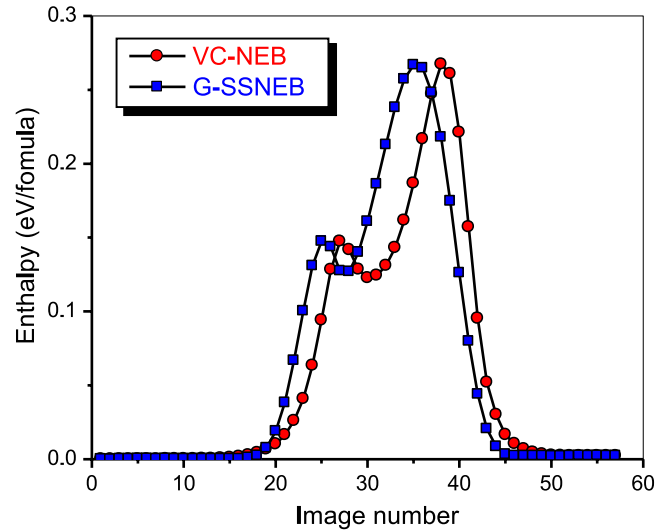
the primary path for the B3 → B1 phase transition is based on a cooperative migration of atom positions from (1/4, 1/4, 1/4) to (1/2, 1/2, 1/2) along the cubic diagonal direction in the B3 phase [31]. All 27 intermediate images are generated by simple linear interpolation. After carrying out the VC-NEB procedure, a transition path (including the atomic positions in the intermediate images and the dependence of H on image number) is obtained through the VC-NEB calculations. Fig. 8(a) shows H as a function of image number for the obtained transition path. It is clear that there are three enthalpy barriers (with almost the same barrier of 0.57 eV/formula and with their peaks located at Images 6, 15 and 25). Correspondingly, there are two minimum enthalpy positions located at Images 11 and 21, i.e., points B and C in Fig. 8(a). After the geometry optimization, the exact structures at Images 11 and 21 are shown in panels B and C in Fig. 8(b), which correspond to the B1 and B3 structures (with the respective orthorhombic [31]
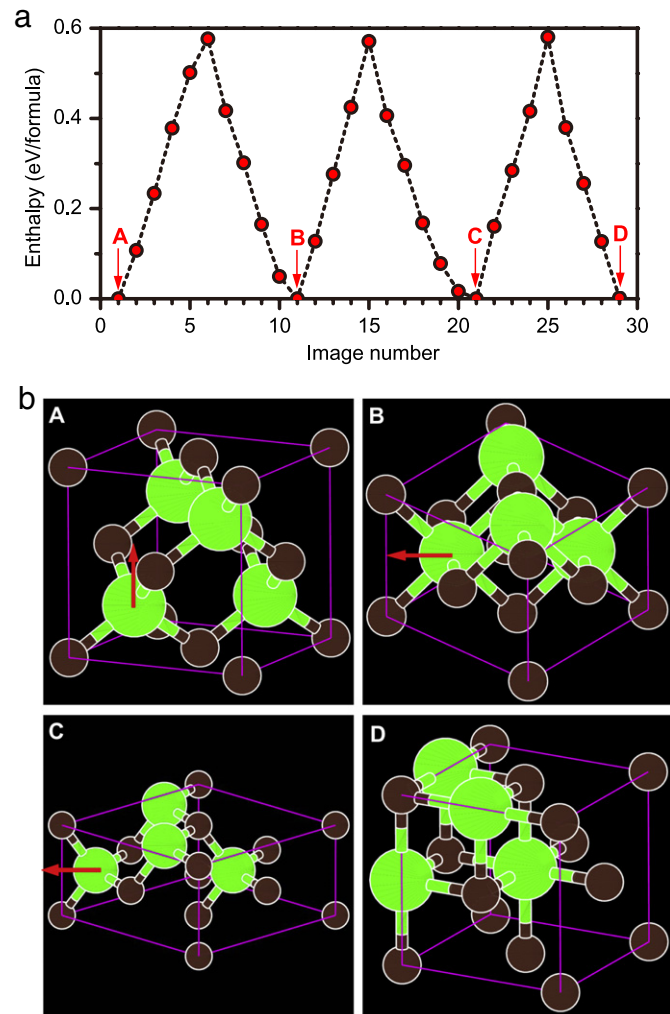
Fig. 8. (Color online) Enthalpy barrier of B3 → B1 phase transition in GaN at the equilibrium pressure 45.0 GPa. At Images 11 and 21, B1 and B3 structures in a monoclinic cell are found during the MEP searching, respectively. The Ga atoms move along the arrow directions during the phase transition.

and monoclinic [32,34] structures), respectively. We also confirm that the phase transition path from the initial image (B3 structure) to Image 11 (B1 structure) goes through the common subgroup *Imm*2, consistent with the results reported in Refs. [31–33,35]. The VC-NEB calculations indicate that the B3 → B1 transition path should be from (1/4, 1/4, 1/4) to (1/4, 1/4, 1/2) as shown from Panel A to Panel B in Fig. 8(b), instead of the above supposed path from (1/4, 1/4, 1/4) to (1/2, 1/2, 1/2). Similarly, the transformations from Image 11 (B1 structure) to Image 21 (B3 structure) and from Image 21 to Image 29 (B1 structure) also contain the transition state with the *Imm*2 space group. We also explore the B3 → B1 phase transition in AlN, and obtain similar results with the enthalpy barrier of 0.34 eV/formula and *Imm*2 transition state [35].

5. Phase transitions pathway in high pressure solid B–H system

Above, using the example of GaN, we have shown that the VC-NEB method is a good way for studying mechanisms of pressure-induced phase transitions. In this section, we investigate a 2D insulator–3D metal structural transformation of BH at high pressure.

Solid B–H compounds are important because of potential application as high-energy-density materials and potential high-temperature superconductors. Recently, it was predicted [45] that

the simplest stable boron hydride at ambient conditions, diborane (B_2H_6), at pressures above 153 GPa breaks down into *Ibam*-BH and H_2. The *Ibam* phase of BH is insulating and has a layered structure. At 168 GPa it was predicted to transform into a $P6/mmm$ structure, which is metallic and has a 3D-connected topology. The VC-NEB method has helped us to study the mechanism of this transition.

For every image, we use a cell containing eight formula units. For greater confidence, we explored several initial pathways between the initial (*Ibam*) and final (*P6/mmm* shape cell) structures with the linear interpolation method and manual configurations [46]. The electronic structure calculations were carried out within the generalized gradient approximation (PBE96 functional) [47] using the projector augmented wave (PAW) method as implemented in the VASP code. We use the plane-wave kinetic energy cutoff of 540 eV and Γ-centered Monkhorst–Pack meshes with reciprocal space resolution of $2\pi \times 0.03$ Å. After performing the VC-NEB calculations, all initial pathways converged to the same one, which features the *Pbcm* structure as a transition state. Fig. 9 shows the enthalpy profile for this transition from the VC-NEB results. In the first stage (*Ibam* → *Pbcm*) of the transition, antiparallel BH-layers are reconstructed into a "parallel" arrangement (see Fig. 9(b)), with a 0.32 eV/formula enthalpy barrier. Then the interlayer distance is decreased (until B–H–B bonds connecting these layers are formed) and layers gradually become flat in the $P6/mmm$ structure. This stage has a much lower enthalpy barrier 0.19 eV/formula. This mechanism implies that low-temperature
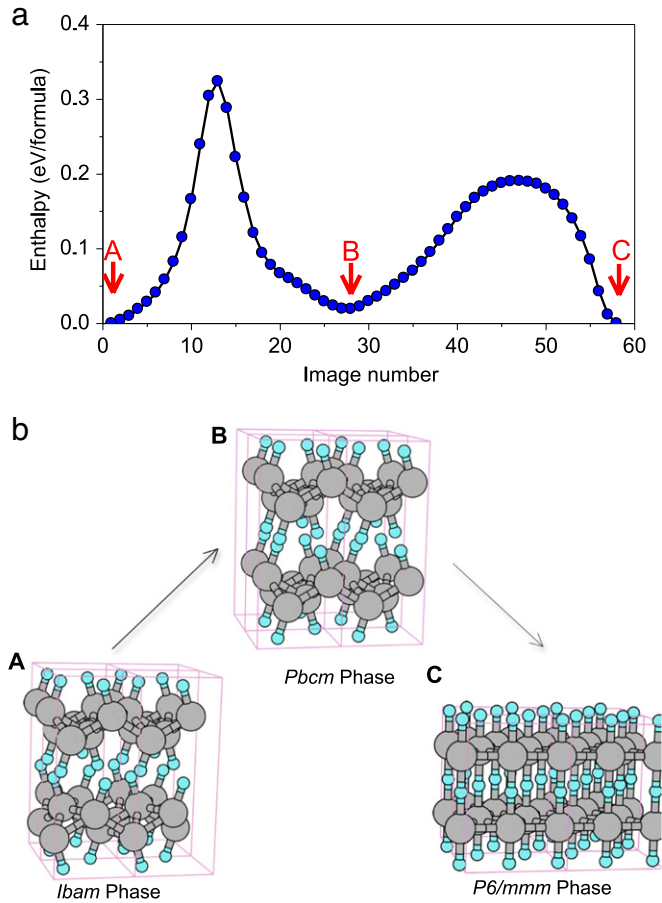
Fig. 9. (Color online) The *Ibam* → *P*6/*mmm* transition of the BH system at 168 GPa. A *Pbcm* intermediate phase is revealed. The saddle points on *Ibam* → *Pbcm* and *Pbcm* → *P*6/*mmm* segments have barriers of 0.32 and 0.19 eV/formula, respectively .

decompression of the *P*6/*mmm* phase may lead to the *Pbcm* structure, rather than the *Ibam* structure.

6. Further discussion

The VC-NEB method is very efficient for finding the phase transition path, but we must also carefully prepare the initial path as in other methods. The cell rotations happen near the initial and final structures during the VC-NEB calculation, a problem that did not occur in a traditional fixed-cell NEB method. This is caused by the change of lattice vectors **h** upon whole-cell rotation, while the structure and energy are invariant to such rotations. To remove these useless rotations, the rotation-avoiding technique needs to be considered in the VC-NEB method when generating the initial image set. The general 3×3 rotation matrix with Euler angles $R(\phi, \theta, \psi)$ and the lattice mirror operator $M(x, y, z)$ matrix are defined. Before performing a VC-NEB calculation, the global numerical search in space of Euler angles and mirror operator are used to find the minimal lattice cell transformation distance Δh

$$\Delta h = \left| h_{initial} - R(\phi, \theta, \psi)M(x, y, z)h_{final} \right| . \tag{8}$$

The rotation-avoiding lattice vector of the final image $\tilde{h}_{final}$ is assigned as the endpoint image

$$\tilde{h}_{final} = R(\phi, \theta, \psi)M(x, y, z)h_{final}. \tag{9}$$

At the same time, we need to prevent the arbitrariness assigning the atomic fractional coordinates $\mathbf{r}_v$ of the initial and final images.

Otherwise, the calculation will be hard to converge or several identical paths can be found in a calculation, as shown in Fig. 8. Global numerical search for minimizing the distance between the atoms from two endpoint images helps the VC-NEB method to reassign the atom sequence. The ability to automatically create model paths before the VC-NEB calculation is crucial for the stability and convergence of the algorithm, and is a prerequisite for studying the large and complex systems.

Compared with the powerful transition path sampling approach [48], the VC-NEB method is a simpler and time-saving method for studying phase transitions. Metastable pressure-induced transitions of graphite were recently studied with the VC-NEB method [49], the transition path sampling method [50] and the climbing-image NEB method [51].

In particular, for complex structural transitions, revealing the mechanism of the phase transition will become quite difficult. Even in simple structures, two or more MEPs may exist between the given initial and final images. The final MEP will likely converge to the path closest to the initial guess by using the minimization technique described above, despite the fact that the found path may not have globally the lowest barrier. The VC-NEB method is a zero-temperature method. Stochastic sampling or molecular dynamics technologies must be introduced into the VC-NEB method to overcome this limitation [3]. Another limitation is that the mean-field picture based on simulations with small supercells gives only a qualitative picture; for physically rigorous calculations of energy barriers of first-order phase transitions, it is necessary to account for nucleation. Both these issues (global search for transition path and accounting for nucleation) are addressed in the transition path sampling method.

For the transition path sampling approach, it is necessary to have a trial trajectory, connecting the initial and final states. There is no general recipe for modeling an initial path in complex systems. After the initial path is successfully found, a shooting-and-shifting procedure evolves the transition path, searching for the globally optimal trajectory. The VC-NEB method gives an excellent initial trajectory for the transition path sampling, avoiding the hard-to-use geometric/topologic approach that has been used before [52].

7. Conclusion

We presented an improved NEB method – the VC-NEB method – allowing unit cell variation, which makes NEB applicable to phase transitions. The frame and procedure of the VC-NEB calculations are described in detail. As examples, we carefully investigated the B4 → B1 and B3 → B1 transitions in GaN. The results confirmed that the B4 → B1 phase transition in GaN prefers the tetragonal transition path instead of the hexagonal one. The phase transitions in ZnO and AlN follow very different paths. The VC-NEB method is a robust and efficient technique for studying phase transitions in solids. Moreover, we have predicted a non-trivial transition mechanism for the newly predicted phases of boron monohydride (BH).

The VC-NEB method and the transition path sampling approach are highly complementary for studying the reconstructive phase transition. Our VC-NEB code is available from G.R.Q. and is also a part of the USPEX code [10] distributed at http://han.ess.sunysb.edu/~USPEX.

References

[1] M.A. Rubio, A. Muñoz, R.J. Needs, Rev. Modern Phys. 75 (2003) 863.
[2] G. Mills, H. Jónsson, G.K. Schenter, Surf. Sci. 324 (1995) 305;
G. Mills, H. Jónsson, K.W. Jacobsen, in: B.J. Berne, G. Ciccotti, D.F. Coker (Eds.), Classical and Quantum Dynamics in Condensed Phase Simulations, World Scientific, Singapore, 1998 (Chapter 16).
[3] G. Henkelman, B.P. Uberuaga, H. Jónsson, J. Chem. Phys. 113 (2000) 9901;
G. Henkelman, H. Jónsson, J. Chem. Phys. 113 (2000) 9978.
[4] D. Sgeppard, R. Terrell, G. Henkelman, J. Chem. Phys. 128 (2008) 134106.
[5] J. Song, L.R. Corrales, G. Kresse, H. Jónsson, Phys. Rev. B 64 (2001) 134102.
[6] P. Maragakis, S.A. Andreev, E. Kaxiras, J. Chem. Phys. 117 (2002) 4651.
[7] S.A. Trygubenko, D.J. Wales, J. Chem. Phys. 120 (2004) 2082.
[8] K.J. Caspersen, E.A. Carter, Proc. Natl. Acad. Sci. 102 (2005) 6738.
[9] D. Sgeppard, P. Xiao, W. Chemelewski, D. Johnson, G. Henkelman, J. Chem. Phys. 136 (2012) 074103.
[10] A.R. Oganov, C.W. Glass, J. Chem. Phys. 124 (2006) 244704.
[11] B.G. Pfrommer, M. Côté, S.G. Louie, M.L. Cohen, J. Comput. Phys. 131 (1997) 233.
[12] M. Parrinello, A. Rahman, Phys. Rev. Lett. 45 (1980) 1196.
[13] R.M. Wentzcovitch, Phys. Rev. B 44 (1991) 2358.
[14] O.H. Nielsen, R. Martin, Phys. Rev. B 32 (1985) 3780.
[15] R. Martin, Electronic Structure, Cambridge, 2004.
[16] T.F. Middleton, D.J. Wales, J. Chem. Phys. 118 (2003) 4583.
[17] W. Quapp, D. Heidrich, Theoret. Chim. Acta (Berl.) 66 (1984) 245.
[18] S. Baroni, et al. Quantum ESPRESSO code. http://www.quantum-espresso.org/.
[19] G. Kresse, J. Furthmüller, Phys. Rev. B 54 (1996) 11169.
[20] J.A. Corll, Phys. Rev. 157 (1967) 623.
[21] M. Wilson, P.A. Madden, J. Phys. Condens. Matter 14 (2002) 4629.
[22] S. Limpijumnong, W.R.L. Lambrecht, Phys. Rev. Lett. 86 (2001) 91.
[23] S. Limpijumnong, S. Jungthawan, Phys. Rev. B 70 (2004) 054104.
[24] A.M. Saitta, F. Decremps, Phys. Rev. B 70 (2004) 035214.
[25] F. Shimojo, S. Kodiyalam, I. Ebbsjo, R.K. Kalia, A. Nakano, P. Vashishta, Phys. Rev. B 70 (2004) 184111.
[26] H. Sowa, Acta Crystallogr. Sect. A 57 (2001) 176;
H. Sowa, Acta Crystallogr. Sect. A 61 (2005) 325.
[27] S.E. Boulfelfel, D. Zahn, Yu. Grin, S. Leoni, Phys. Rev. Lett. 99 (2007) 125505.
[28] J. Cai, N. Chen, Phys. Rev. B 75 (2007) 134109.
[29] F. Shimojo, I. Ebbsjo, R.K. Kalia, A. Nakano, J.P. Rino, P. Vashishta, Phys. Rev. Lett. 84 (2000) 3338.
[30] M.A. Blanco, J.M. Recio, A. Costales, R. Pandey, Phys. Rev. B 62 (2000) R10599.
[31] M. Catti, Phys. Rev. Lett. 87 (2001) 035504; Phys. Rev. B 65 (2002) 224115; Phys. Rev. Lett. 90 (2003) 049604.
[32] M.S. Miao, M. Prikhodko, W.R.L. Lambrecht, Phys. Rev. B 66 (2002) 064107; Phys. Rev. Lett. 88 (2002) 189601;
M.S. Miao, W.R.L. Lambrecht, Phys. Rev. B 68 (2003) 092103; Phys. Rev. Lett. 94 (2005) 225501.
[33] J.M. Perez-Mato, M. Aroyo, C. Capillas, P. Blaha, K. Schwarz, Phys. Rev. Lett. 90 (2003) 049603.
[34] D.M. Hatch, H.T. Stokes, J. Dong, J. Gunter, H. Wang, J.P. Lewis, Phys. Rev. B 71 (2005) 184109.
[35] R.F. Zhang, S.H. Sheng, S. Veprek, Phys. Rev. B 76 (2007) 075208.
[36] J.P. Perdew, J.A. Chevary, S.H. Vosko, K.A. Jackson, M.R. Pederson, D.J. Singh, C. Fiolhais, Phys. Rev. B 46 (1992) 6671;
J.A. White, D.M. Bird, Phys. Rev. B 50 (1994) 4954.
[37] D. Vanderbilt, Phys. Rev. B 41 (1990) 7892.
[38] N. Troullier, J.L. Martins, Phys. Rev. B 43 (1991) 1993.
[39] J.E. Jaffe, J.A. Snyde, Z. Lin, A.C. Hess, Phys. Rev. B 62 (2000) 1660.
[40] J. Serrano, A. Rubio, E. Hernández, A. Muñoz, A. Mujica, Phys. Rev. B 62 (2000) 16612.
[41] C.C. Silva, H.W. Leite Alves, L.M.R. Scolfaro, J.R. Leite, Phys. Status Solidi C 2 (2005) 2468.
[42] W. Shan, B.D. Little, A.J. Fischer, J.J. Song, B. Goldenberg, W.G. Perry, M.D. Bremser, R.F. Davis, Phys. Rev. B 54 (1996) 16369.
[43] S. Nakamura, Science 281 (1998) 956.
[44] The enthalpy barrier for the B4 → B1 phase transition of AlN was calculated by using both the VC-NEB and G-SSNEB methods (VTST code, http://theory.cm.utexas.edu/vtsttools/) at $P_t = 14.0$ GPa in a four-atom cell. All the electronic structure calculations were carried out with the projector augmented wave (PAW) method as implemented in the VASP code. The PW91 GGA exchange-correlation functional was used in the VC-NEB and G-SSNEB calculations at the transition pressure, with a plane-wave cutoffs of 450 eV and a $6 \times 6 \times 4\Gamma$-centered Monkhorst–Pack k-point grids. 57 images and the climbing image NEB were implemented in both the VC-NEB and G-SSNEB calculations with no rotation-avoiding technique. The phase transition barrier for the VC-NEB calculation is 0.265 eV/formula and the G-SSNEB method gives the same barrier. The corresponding enthalpy of h-MgO metastable structure from the VC-NEB method is 0.12 eV/formula, which is close to 0.13 eV/formula reported in Ref. [28].
[45] C.H. Hu, A.R. Oganov, Q. Zhu, G.R. Qian, A.O. Lyakhov, H.Y. Zhou, Phys. Rev. Lett. 110 (2013) 165504.
[46] Manual configurations as $\mathbf{X_1} = (\varepsilon_{Ibma}; \mathbf{r}_{P6/mmm})$ and $\mathbf{X_2} = (\varepsilon_{P6/mmm}; \mathbf{r}_{Ibma})$ are set as the intermediate phases in the B–H system VC-NEB pathway initialization. ε_{Ibma}, $\varepsilon_{P6/mmm}$, $\mathbf{r}_{P6/mmm}$ and $\mathbf{r}_{Ibma}$ are the finite strain tensors and atomic fractional coordinations of $Ibma$ and $P6/mmm$ B–H phases at 168 GPa respectively.
[47] J.P. Perdew, K. Burke, M. Ernzerhof, Phys. Rev. Lett. 77 (1996) 3865.
[48] P.G. Bolhuis, C. Dellago, P.L. Geissler, D. Chandler, Ann. Rev. Phys. Chem. 54 (2002) 20;
C. Dellago, P.G. Bolhuis, P.L. Geissler, Adv. Chem. Phys. 123 (2002) 1.
[49] X.F. Zhou, G.R. Qian, X. Dong, L.X. Zhang, Y.J. Tian, H.T. Wang, Phys. Rev. B 82 (2010) 134126.
[50] S.E. Boulfelfel, A.R. Oganov, S. Leoni, Sci. Rep. 2 (2012) 471.
[51] J.T. Wang, C. Chen, Y. Kawazoe, Phys. Rev. Lett. 106 (2011) 075501.
[52] S.E. Boulfelfel, D. Zahn, O. Hochrein, Y. Grin, S. Leoni, Phys. Rev. B 74 (2006) 094106.